Inorganica Chimica Acta 582 (2025) 122654

Contents lists available at ScienceDirect

Inorganica Chimica Acta

journal homepage: www.elsevier.com/locate/ica

Targeted drug delivery for Cancer therapy using Cu(bpdc) and Ni(bpdc) - MOFs

A.H. Hatin Betseba [a,1], Y. Brucely [b], G. Paulraj [b], Y. Christabel Shaji [a,*]

[a] Department of Chemistry, Holy Cross College (Autonomous), Nagercoil, Tamil Nadu, India
[b] Department of Mechanical Engineering, SRM TRP Engineering college, Irangalur, Trichirappalli 621105, Tamilnadu, India

ARTICLE INFO

Keywords:
Cu and Ni-based MOFs
Photocatalytic degradation
Congo red
Cisplatin
Drug delivery
Cancer

ABSTRACT

Metal-Organic Frameworks (MOFs) have emerged as potentially useful porous materials due to their high surface area, ordered porous structure and versatility in the field of drug delivery and photocatalysis. Understanding the molecular and structural interactions that enable these MOFs to exhibit both high photocatalytic activity and effective drug delivery remains a key challenge. This study highlights the synthesis and evaluation of Cu and Ni-based metal-organic frameworks (MOFs) using biphenyl-4,4′-dicarboxylic acid as a ligand and DMF as a solvent via a hydrothermal method in a stainless-steel Teflon autoclave. The Cu(bpdc)-MOF and Ni(bpdc)-MOF demonstrated exceptional degradation efficiencies for congo red under UV–Visible light, achieving 99 % and 97 % degradation at 140 and 160 min, respectively. This highlights their potential for environmental remediation. Furthermore, these MOFs, when loaded with cisplatin through a simple impregnation method, exhibited significant cytotoxicity against breast cancer MDA-MB-231 cells, with cell viabilities of 37.63 % and 40.7 % at the higher concentration of 100 μg/mL with the IC_{50} values of 55.78 μg/mL and 62.15 μg/mL. However, challenges remain in optimizing the synthesis process to improve reproducibility and scalability and further understanding the interactions governing their dual functionality in photo catalysis and drug delivery. These findings offer valuable insights into the development of multifunctional MOFs for environmental and biomedical applications.

1. Introduction

Metal-organic frameworks (MOFs) represent a category of porous crystalline materials that consist of metal ions or clusters linked to organic ligands. Their exceptionally high surface area, adjustable pore sizes, and varied chemical functionalities render them valuable across numerous applications and also that can be one-, two- or three-dimensional. Their highly tunable nature, enabled by variation in metal nodes and organic linkers, allows for the design of materials with diverse structural and functional properties [1]. MOFs are particularly attractive due to their high surface area, controllable porosity, structural stability and ease of synthesis, making them promising candidates for applications in drug delivery [2], adsorption [3], catalysis [4] and sensing [5]. Water pollution, a critical environmental issue, is a significant challenge in developing nations, where contaminants in wastewater pose severe ecological and health risks [6]. Among these contaminants, azo dyes are widely used synthetic dyes that account for over two-thirds of global dye production. These dyes are often toxic, mutagenic and carcinogenic, with metabolites that can be readily absorbed by the human body, contributing to adverse health outcomes [7,8]. The World Health Organization (WHO) reported that over 700,000 tons of synthetic dyes were produced globally last year, with a large fraction released into the environment through industrial effluents [9]. Current dye removal methods, such as Fenton's oxidation [10], adsorption [11], coagulation-flocculation [12], biological treatment [13] and membrane filtration [14] often have limitations in efficiency, scalability or environmental impact. Photocatalysis has emerged as a highly effective approach for degrading organic pollutants, including dyes, by utilizing photocatalytic semiconductors and UV–visible light. Unlike traditional methods, photocatalysis operates under mild conditions without requiring expensive oxidants [15]. Common photocatalysts include TiO_2, ZnO, WO_3, carbon-based materials and MOFs [16–20]. It has attracted interest as innovative photocatalysts because of their capacity to integrate various functional components into a single

---

[*] Corresponding author.
E-mail address: christabelshaji@holycrossngl.edu.in (Y.C. Shaji).

[1] Affiliated to Manonmaniam Sundaranar University, Tirunelveli-629 004.

https://doi.org/10.1016/j.ica.2025.122654
Received 24 October 2024; Received in revised form 2 March 2025; Accepted 13 March 2025

material [21]. For example, MOFs such as Co, Ni and Zn-based frameworks have shown excellent performance in degrading dyes like methylene blue and rhodamine B [22]. Additionally, Ln-MOFs (Ce, Tb, Dy) have demonstrated efficient photoinduced charge production and visible light absorption for the degradation of RhB [23].

Cancer continues to be a primary cause of death globally, with breast cancer ranking as the most commonly diagnosed cancer in women [24]. Triple-negative breast cancer (TNBC), characterized by its aggressive phenotype and poor prognosis, is particularly challenging to treat [25]. Although chemotherapy is the primary treatment, its non-specific action often causes systemic side effects and damages healthy cells. To address these limitations, the fields of nanobiotechnology and nanomedicine have advanced rapidly, leading to the development of nanoscale drug delivery systems (DDSs) that enhance therapeutic efficacy while minimizing side effects [26,27]. MOFs have recently emerged as promising nanocarriers for cancer therapy due to their unique properties. Their nanoscale size facilitates drug absorption, while the selection of biocompatible metals and organic linkers minimizes toxicity. Additionally, their high porosity enables substantial drug loading and their biodegradability ensures controlled release of therapeutic agents [28]. For instance, ZIF-8-based MOFs have been utilized to deliver anticancer drugs through pH-responsive mechanisms, exploiting the acidic microenvironment of tumor sites [29]. Similarly, ZJU-101 MOFs have demonstrated effective drug release via electrostatic interactions between charged drugs and MOF carriers [30]. These advancements highlight the potential of MOFs as multifunctional materials for applications in environmental remediation and cancer therapy.

Herein, we report the synthesis of Cu(bpdc)-MOF and Ni(bpdc)-MOF photocatalyst which is synthesized by the hydrothermal method in stainless steel Teflon autoclave. Experiments reveal that the Cu(bpdc)-MOF and Ni(bpdc)-MOF is a highly efficient photocatalysts for Congo red degradation on exposure to UV–visible light. Moreover, the incorporation of cisplatin inside Cu(bpdc)-MOF and Ni(bpdc)-MOF by liquid impregnation method made the synthesized products as an anticancer drug delivery system against breast cancer MDA-MB-231 line.

2. Materials and methods

2.1. Chemicals

Nickel chloride hexahydrate, copper sulphate pentahydrate, biphenyl-4,4′-dicarboxylic acid, sodium hydroxide, dimethyl formamide, cisplatin, Congo red. All chemicals utilized in this study are sourced from Sigma Aldrich and employed without additional purification. The MDA-MB-231 breast cancer cell line was purchased from the National Centre for Cell Sciences situated in Pune, India.

2.2. Synthesis of Cu(bpdc)-based MOF

The synthesis of Cu(bpdc)-MOF was carried out by hydrothermal method in a stainless-steel Teflon autoclave. About 1.001 mmol of $CuSO_4.5H_2O$ is dissolved in 20 mL of deionized water (sol A) and 1 mmol biphenyl-4,4′-dicarboxylic acid is dissolved in 20 mL of dimethyl formamide (sol B). Sol A is slowly added to sol B and 0.2 g of NaOH is added to the homogenizing stirring solution at room temperature for 1 h. The reaction was carried out in a 100 mL Teflon sample container with a stainless-steel protective cover and heated at 185 °C for 8 h in the reactor. After the reaction was completed, the product was allowed to cool naturally. Then the product is washed with DMF thrice. Finally, the obtained product is dried at 100 °C for 4 h [31].

2.3. Synthesis of Ni(bpdc)-based MOF

The synthesis of Ni(bpdc)-MOF is achieved through the exertion of the hydrothermal method, where 1.010 mmol of $NiCl_2.6H_2O$ is dissolved in 20 mL of deionized water (sol A) and 1 mmol of biphenyl-4,4′-dicarboxylic acid is dissolved in 20 mL of DMF (sol B). Sol A is added slowly to sol B and 0.2 g of NaOH is added and stirred for 1 h at room temperature. The solution is then transferred into a 100 mL Teflon autoclave and heated at 185 °C for 8 h. The resulting product is filtered after cooling at room temperature and then washed three times with DMF. Finally, the product obtained is dried at 100 °C for 4 h [32].

2.4. Encapsulation of cisplatin inside MOFs

Cisplatin encapsulation was performed by a simple impregnation method. Approximately 500 mg of Cu(bpdc)-MOF and Ni(bpdc)-MOF powder was suspended in cisplatin solution (2.4 mg/mL) and stirred continuously for 72 h at room temperature. After a certain time period, the solvent was removed by centrifugation. Before the loading of cisplatin, the MOFs were dried in an oven to remove the water molecules. The cisplatin-loaded Cu(bpdc)-MOF and Ni(bpdc)-MOF were evaluated against the breast cancer MDA-MB-231 cell line and normal L-929 cell line.

2.5. Catalyst characterization

The composite synthesis and crystal phase change were identified by XRD analysis using a Bruker binary V4 X-ray diffractometer with Cu Kα (1.5406 Å) irradiation in the range of 0–80°. The existence of functional collections on the outer surface of material in the wavelength of 400–4000 cm^{-1} was ascertained by Fourier transform infrared spectra (FTIR) from SHIMADZU IR Affinity-1. The investigation of the particle morphology of the samples was conducted using transmission electron microscopy (TEM) with a JEOL-2100+ instrument working at 200Kv and scanning electron microscopy with a Quanta FEG-250 equipped with an EDS attachment. Thermofisher assessment 220 was utilized to obtain the UV–Visible DRS spectra of materials in the range of 300–800 nm to identify the catalysts absorption peaks, which ranged in wavelength from 100 nm to 1100 nm. Using a Quantachrome Nova 1200, the surface area of the produced products was determined using the N_2 sorption isotherm. During the photocatalysis process, the concentration of organic pigment solution was measured using a UV–Vis instrument UV-1800 Series with wavelength of 340 nm. Using PHI-VERSAPROBE III, X-ray photoelectron spectroscopy for elemental analysis was recorded.

2.6. Dye degradation

In order to test the photocatalytic activity of Cu(bpdc)-MOF and Ni (bpdc)-MOFs, the photocatalytic degradation of Congo red in the suspension of aqueous solution under UV–Vis light irradiation was studied. A 500 W mercury vapour lamp was fixed at a distance of 45 cm above the surface solution and the whole instrument was set in a sealed lightbox. About 0.002 g of Congo red is dissolved in 1000 mL of double-distilled water to create a solution. About 0.05 g of the photocatalysts as made are added to 40 mL of dye solution in a standard photocatalytic experiment. Prior to light irradiation, the reaction mixture is agitated for 30 min in the absence of light to achieve sorption equilibrium between the dye molecules and the catalyst surface. Then 4 mL of the mixture is taken out at regular time intervals and measured the absorbance. Finally, UV–vis absorption analysis is conducted to evaluate the concentration of congo red solution through the decrease in colour concentration, expressed by the change in the maximum absorption peak intensity under the effect of light.

2.7. Cell culture and maintenance

Following a 24-h exposure to the MOF formulations, the breast cancer MDA-MB-231 cell line and normal L-929 cell line exhibited activation. Dulbecco’s Modified Eagle’s Medium (DMEM-Himedia) serves as the growth medium for cell culture applications. The medium is enriched with 10 % heat-inactivated Foetal Bovine Serum (FBS) and includes 1 % antibiotic cocktail composed of streptomycin (100 µg/mL), penicillin (100 U/mL) and amphotericin B (2.5 µg/mL). A cell culture incubator (Galaxy ® 170, Eppendorf, Germany) was utilized to maintain cells in tissue culture (TC) flasks (25 cm^2) at 37 °C and 5 % CO_2.

2.8. *Preparation of cytotoxicity by MTT assay*

MTT assay was assessed from the perspective of in-vitro cell viability of Cis@Cu(bpdc)-MOF and Cis@Ni(bpdc)-MOF. The standard protocol involved choosing breast cancer MDA-MB-231 and normal L-929 cells, seeding them into 96-well plates at a density of 2500 cells/well in 200 µL of cell medium and then incubating them for the entire night at 37 °C with 5 % CO_2. Before receiving treatment, the cell monolayers were cleaned with PBS. Cis@Cu(bpdc)-MOF and Cis@Ni(bpdc)-MOF were applied to the cells at varying durations and concentrations. Following this, MTT solutions (5 mg/mL) were added to each well and incubated for an additional 4 h at 37 °C. Following a four-hour incubation period, the growth media was removed and 200 µL of DMSO solvent was introduced to each well to facilitate the dissolution of the formazan crystals. The optical density at 570 nm was measured using an ELISA microplate reader. The outcomes were analysed in relation to control cells that solely included cell-cultured media and the culturing experimentations were conducted 3 times [32].

3. Results and discussion

3.1. *XRD analysis*

Using Cu Kα radiation at a wavelength of 1.5406 Å, the X-ray Diffraction (XRD) spectra of Cu(bpdc)-MOF and Ni(bpdc)-MOF were recorded. An extensive examination of the crystal phase of Cu(bpdc)-MOF and Ni(bpdc)-MOF was conducted across a spectrum of diffraction angles (2θ) ranging from 10 to 80 degrees. The XRD spectra of Cu (bpdc)-MOF displayed distinct characteristics, as indicated by the peaks illustrated in Fig. 1(a) and also it shows that Cu(bpdc)-MOF shows crystalline nature and Ni(bpdc) shows amorphous nature. High-intensity diffraction peaks were observed at $2\theta = 19.01$ and 32.10, which correspond to the (101) and (103) planes, respectively. In a similar manner, the XRD spectra of Ni(bpdc)-MOF exhibited clear peaks at 12.93, 20.45 and 24.81. The mean crystalline size was determined using the Scherrer eq. (See Table 1.)

$D = k\,\lambda\,/\,\beta\ \mathrm{Cos}\theta.$

Where, λ is the wavelength of X-ray source (1.506 Å), K is the Scherrer constant (0.98), D is the crystallite size, θ is the Bragg angle and β is the full-width half maximum (FWHM) in radians. The average size of Cu(bpdc)-MOF and Ni(bpdc)-MOF was 45.18 and 20.3 nm [33–38].

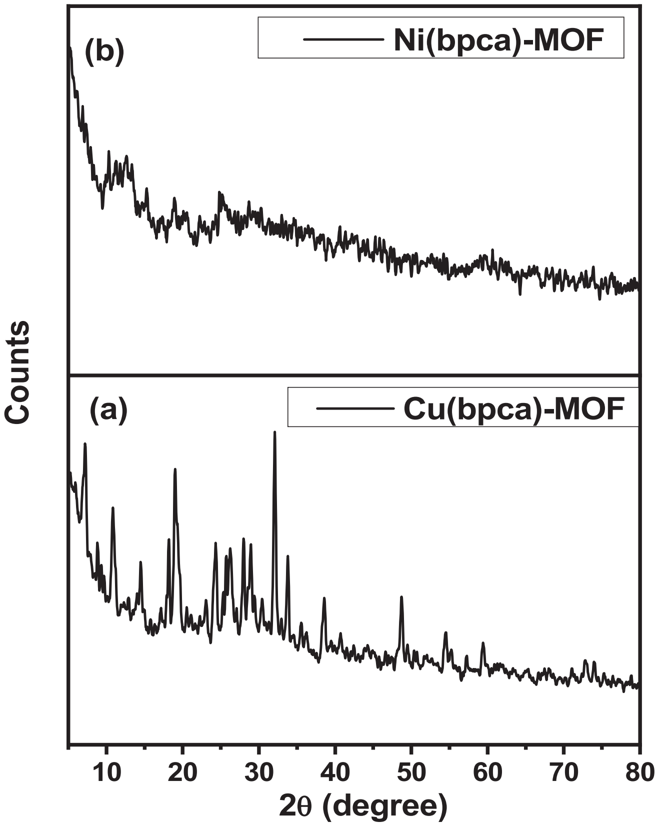

Fig. 1. **(a)**XRD of Cu(bpdc)-MOF and **(b)** Ni(bpdc)-MOF.

Table 1
MTT assay of Cis@Cu(bpdc)-MOF and Cis@Ni(bpdc)-MOF on MDA-MB-231.

Concentrations (µg/mL)	Cis@Cu(bpdc)-MOF		Cis@Ni(bpdc)-MOF	
	Cellular viability (%)	Growth inhibition (%)	Cellular viability (%)	Growth inhibition (%)
6.25	94.02	5.98	94.2	5.8
12.5	77.92	22.08	79.78	20.22
25	62.76	37.24	63.47	36.53
50	47.20	52.8	50.4	49.6
100	37.63	62.37	40.7	59.3

3.2. *SEM with EDX analysis*

Scanning electron microscopy is a technique that enables to examine the microstructure and morphology of the synthesized products. SEM images of Cu(bpdc)-MOF and Ni(bpdc)-MOF are displayed in the fig.(2). SEM micrographs show the distribution of particles in Cu(bpdc)-MOF and Ni(bpdc)-MOF with a range of dimensions and were captured at different magnifications. The SEM images of Cu(bpdc)-MOF presented in Fig. 2(a&b) show their formation as small, sharp and clusters of needle-shaped crystals. A high degree of uniformity in the synthesized Cu (bpdc)-MOFs is further suggested by the absence of other morphologies. The purpose of the EDAX study was to ascertain the elemental analysis of the synthesized Cu(bpdc)-MOFs. Fig. 2(c) displays the EDAX analysis results [39]. The SEM image of Ni(bpdc)-MOFs shown in Fig. 2 (d&e) reveals their existence as wire-shaped aggregated to form nest-like structures. Different energy peaks correspond to different elements in EDAX analysis. From Fig. 2(f), the existence of carbon, nitrogen, oxygen and nickel in the synthesized Ni(bpdc)-MOF is confirmed [40].

3.3. *FT-IR analysis*

FT-IR spectroscopy is employed for a more detailed analysis of the presence of functional groups. Fig. 3 illustrates that the absorption band at 3423.56 cm^{-1} corresponds to the asymmetric and symmetric N—H stretching, while the band at 1632.78 cm^{-1} is associated with the asymmetric and symmetric H-N-H stretching in cisplatin [41]. In the case of Cu(bpdc)-MOF, two prominent bands at 685 and 742 cm^{-1} are associated with the vibrational stretching of the C—H group and the deformation vibration of the benzene ring. The four prominent bands at 893, 1434, 1535 and 1585 cm^{-1} are associated with the vibrational stretching of COO^-, which is linked to the metal centre. Among these, the two bands at 1434 and 1585 cm^{-1} are attributed to the symmetric and asymmetric stretching of COO^- groups. The difference between these two bands suggests that by bidentate ligands the COO^- groups are correlated to the metal centre. The broad band at 3589.48 cm^{-1} corresponds to the -OH stretching. The band at 1567 cm^{-1} is assigned to C═C stretching that further validates the existence of benzene ring.

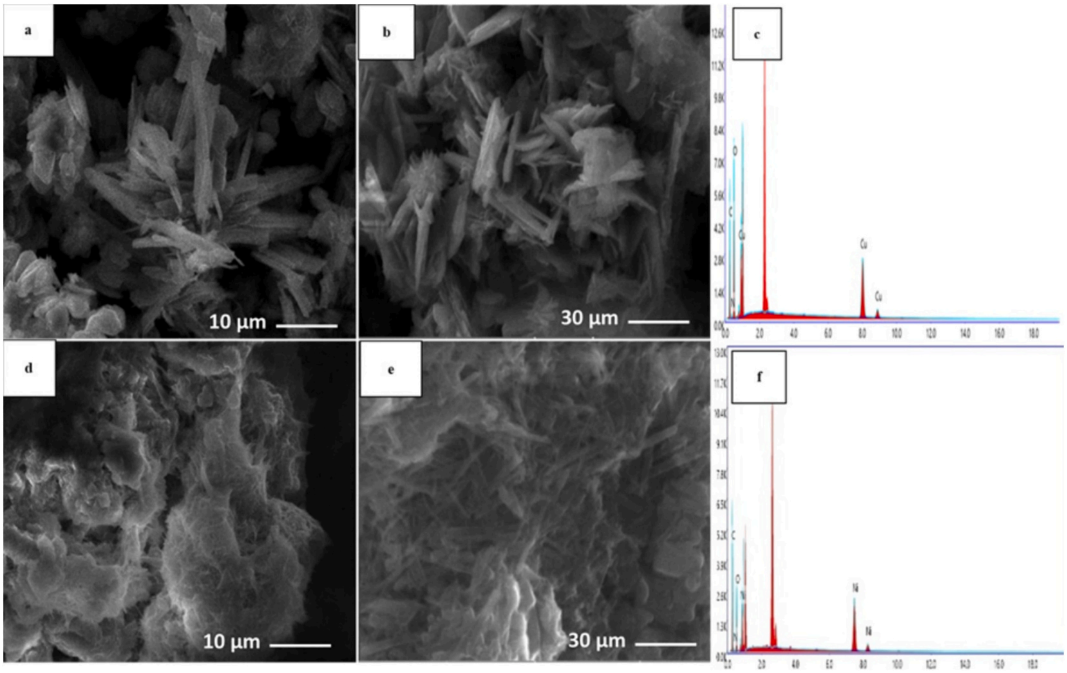

Fig. 2. SEM with EDAX of Cu(bpdc)-MOF (a,b,c) and Ni(bpdc)-MOF (d,e,f).

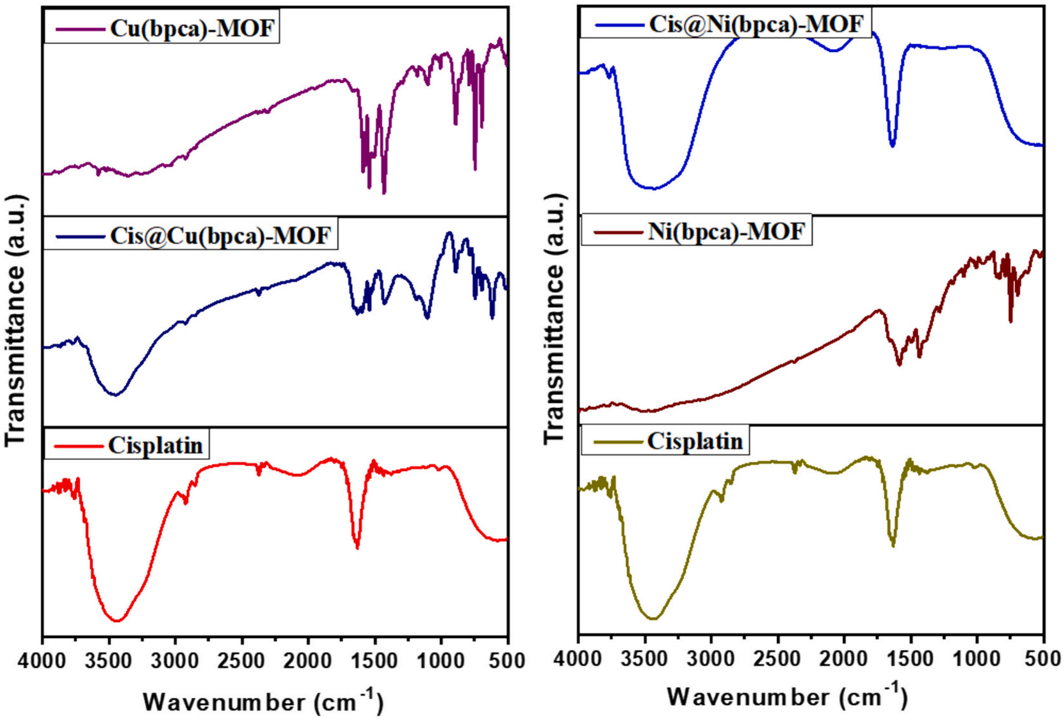

Fig. 3. FT-IR of Cu(bpdc)-MOF and Ni(bpdc)-MOF.

Furthermore, the distinction between the symmetric and asymmetric stretching modes of the coordinated -COO^{-} group enables us to confirm that the -COO^{-} group of bpdc has indeed been coordinated to Cu^{2+}. All Cis@Cu(bpdc)-MOF exhibited distinctive peaks associated with Cu (bpdc)-MOF, alongside a subtle peak of amine stretching at 3274 cm^{-1}, signifying the presence of an unaltered amine group [42].

Similarly, in Ni(bpdc)-MOF, four bands at 846, 1463, 1517 and 1554 cm^{-1} were obtained which corresponds to carboxylate groups (COO^{-}) stretching correlated to the metal centre. The bands at 1463 and 1554 cm^{-1} correspond to symmetric and asymmetric stretching of COO^{-} coordinated to Ni^{2+} centre by bidentate ligand. Two intense bands at 671 and 727 cm^{-1} are attributed to stretching vibration of C—H group and the antiplanar bending vibration of benzene ring. A band observed at 1651 cm^{-1} is ascribed to the stretching of C=C that validates the presence of benzene ring. All Cis@Ni(bpdc)-MOF showed characteristic peaks of Ni(bpdc)-MOF with additional intense peak at 3271 cm^{-1} assigned to weak -NH$_2$ stretching [43].

3.4. UV–Vis DRS analysis

The UV–Vis diffuse reflectance spectroscopy (DRS) approach, which is illustrated in Fig. 4(a&c), is used to examine the optical behavior and energy band structure of Cu(bpdc)-MOF, Cis@Cu(bpdc)-MOF, Ni(bpdc)-MOF and Cis@Ni(bpdc)-MOF. UV–Vis DRS is a spectroscopic technique used to analyze the optical properties of solid materials and measures how a material reflects ultraviolet (UV) and visible (Vis) light rather than transmitting it. This technique is commonly used for studying semiconductor materials, catalysts and pigments. A notable response is suggested by the UV–Vis DRS for Cu(bpdc)-MOF and Ni(bpdc)-MOF, which show an absorption band in the 250-600 nm and 300-700 nm wavelength ranges. The energy needed in a semiconductor to move electrons to the conduction band from the valence band is known as the optical bandgap energy. The energy is computed using the Kubelka-Munk method to convert the reflectance to absorbance in the UV–Vis diffuse reflectance spectra.

$$\frac{K}{S}=\frac{(1-R)^2}{2R}$$

Where K is the molar absorption coefficient, R is the reflectance and S is the scattering factor. The band gaps for Cu(bpdc)-MOF and Ni(bpdc)-MOF were found to be 3.47 eV and 3.63 eV, respectively, based on the plot of $(F(R)h\upsilon)^2(\mathrm{eVcm}^{-1})$ vs energy (eV) and these larger values indicate the semiconductor nature of the synthesized materials and showed good photocatalytic activity under UV–visible light irradiation upon long exposure. For Cu(bpdc)-MOF and Ni(bpdc)-MOF, the absorption edge is shifted to a longer wavelength region, respectively, suggesting that they may be able to absorb visible light in contrast to Cis@Cu(bpdc)-MOF and Cis@Ni(bpdc)-MOF, which displayed a decrease in absorption intensity. Both the coordination bonding of Cu(II)-Cisplatin and Ni(II)-Cisplatin and the electrostatic interaction between the negatively charged carboxylic acid and positively charged Cisplatin are responsible for the high drug-loading capacity of cisplatin in Cu(bpdc)-MOF and Ni(bpdc)-MOF [44,45].

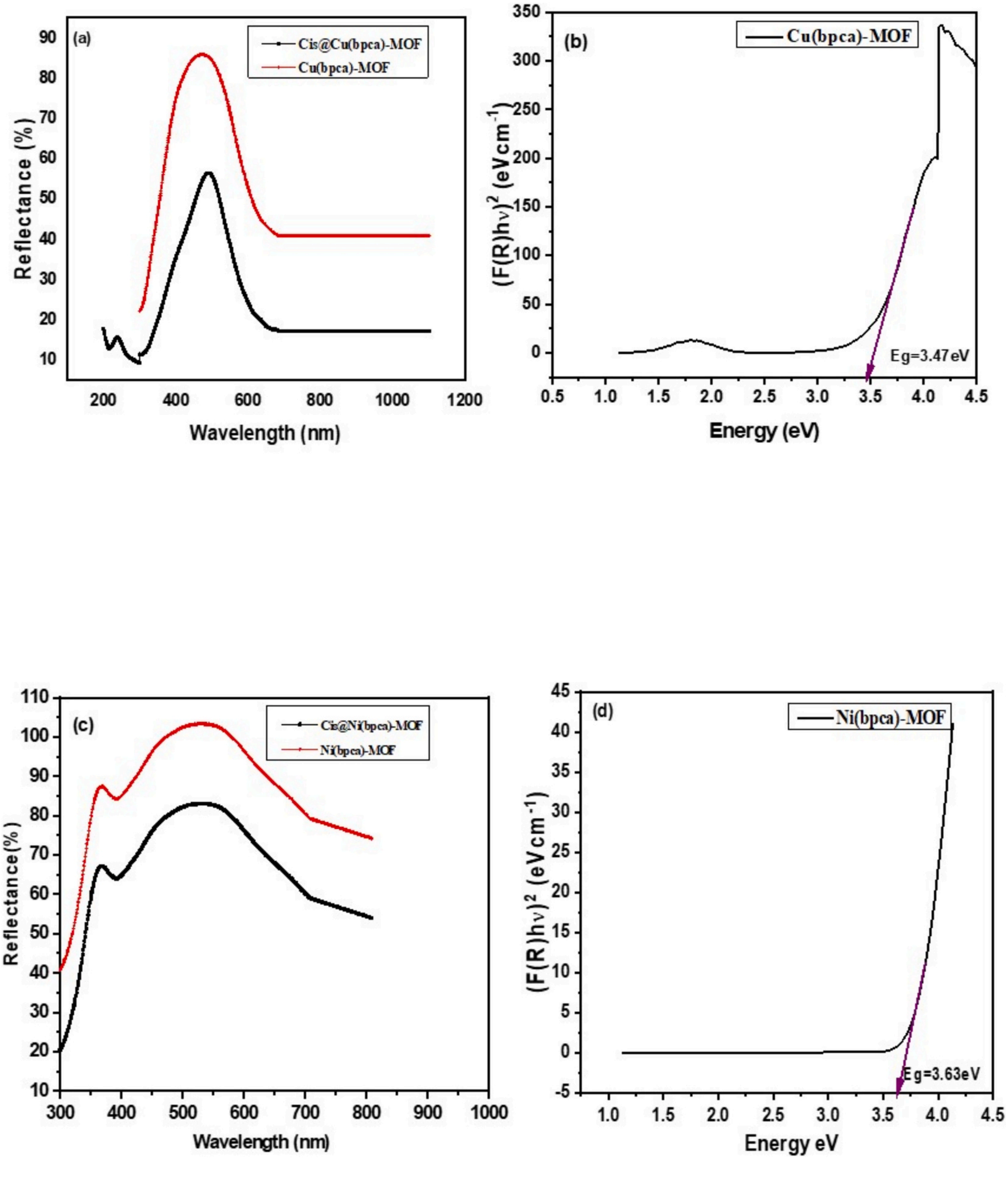

Fig. 4. UV–Vis DRS and bandgap energy of Cu(bpdc)-MOF (a,b) and Ni(bpdc)-MOF (c,d).

3.5. XPS analysis

(f) Ni2p (g) C1s (h) O1s.

A broad XPS survey was conducted to examine the compositions of the synthesized Cu(bpdc)-MOF and Ni(bpdc)-MOF in order to better comprehend the surface information of these materials. Cu(bpdc) MOF was found to be made up of Cu2p3, C1s, O1s and N1s elements based on the XPS survey spectra in Fig. 5(a). The O1s high-resolution XPS spectrum revealed a peak at 530.94 eV ascribed to the -OH group, while the C1s spectrum revealed a peak at 284.77 eV and 288.73 eV, which correspond to the C-C/C═C and C═O of carbonyl groups. Cu2p3 spectra showed four distinct peaks: two at 953.16 eV and 933.9 eV were attributed to Cu2p1/2 and Cu2p3/2, while the other two at 944.36 and 955.2 eV were the satellite peaks of Cu2p3/2 and Cu2p1/2, respectively. Based on these findings, the copper ion exists as Cu^{2+} [46].

The XPS of Ni(bpdc) MOF is shown in Fig. 5(e). Four elemental peaks were identified from the survey spectra, confirming the presence of nitrogen, carbon, oxygen and nickel. Ni2p spectra showed four distinct peaks; two of these peaks at 871.42 eV and 854.83 eV corresponded to Ni2p3/2 and Ni2p1/2. Furthermore, the satellite peaks of Ni2p1/2 and Ni2p3/2 are visible as broad peaks at 861.43 eV and 879.02 eV. These findings from the Ni2p spectra demonstrated that the produced Ni (bpdc)-MOF contains nickel ions in Ni^{2+}. Two peaks were observed at 284.82 eV and 288.47 eV in the C1s spectra, which were assigned to the C═C of benzene ring and the C═O of the carboxylate, respectively. The peak at 530.96 eV in the O1s spectra was assigned to the adsorbed -OH group [47].

3.6. TGA analysis

(d) Cis@Ni(bpdc)-MOF.

To better understand the decomposition mechanism of the synthesized MOFs, the thermal decomposition process was investigated by thermogravimetric analysis. As shown in Fig. 6(a), five mass drops were observed for Cu(bpdc)-MOF, the first drop in mass of 8.71 % happened from room temperature to 92 °C and was caused by the removal of H$_2$O. The corresponding drop in mass of 8.21 %, 8.55 %, and 5.6 % happened between 100 and 380 °C with a massive drop of 29.06 % at 495 °C caused due to the decomposition of Cu(bpdc)-MOF structure. When a temperature above 495 °C was applied, with residue lower than 40 % left behind, the mass persisted to be stable. In the case of Cis@Cu(bpdc)-MOF shown in Fig. 6(b), seven drops in mass were observed. The first five drops in mass happened between room temperature to 400 °C. The highest drop in mass of 24.33 % happened at 440 °C and the lowest drop in mass happened between 565 and 615 °C. When a temperature higher than 615 °C is applied, the mass remains stable with less than 25 % residue left behind. Thermogravimetric analysis revealed that Cu(bpdc)-MOF and Cis@Cu(bpdc) was thermally stable below 380 °C and 440 °C. The thermal stability of Cis@Cu(bpdc)-MOF was higher than that of Cu (bpdc)-MOF [48]. As shown in Fig. 6(d), five mass drop is observed for

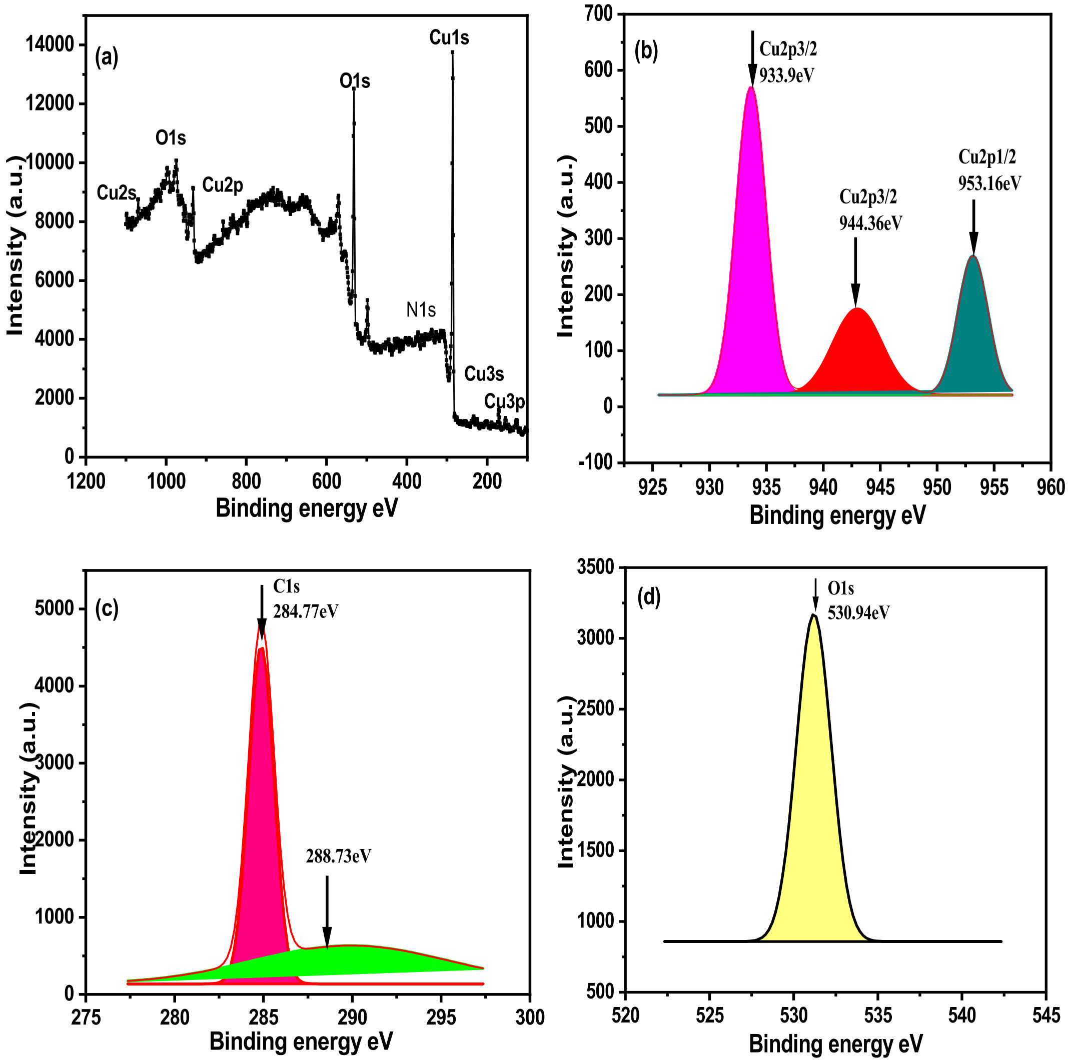

Fig. 5. XPS of (a) Cu(bpdc)-MOF (b) Cu2p (c) C1s (d) O1s and (e) Ni(bpdc)-MOF.

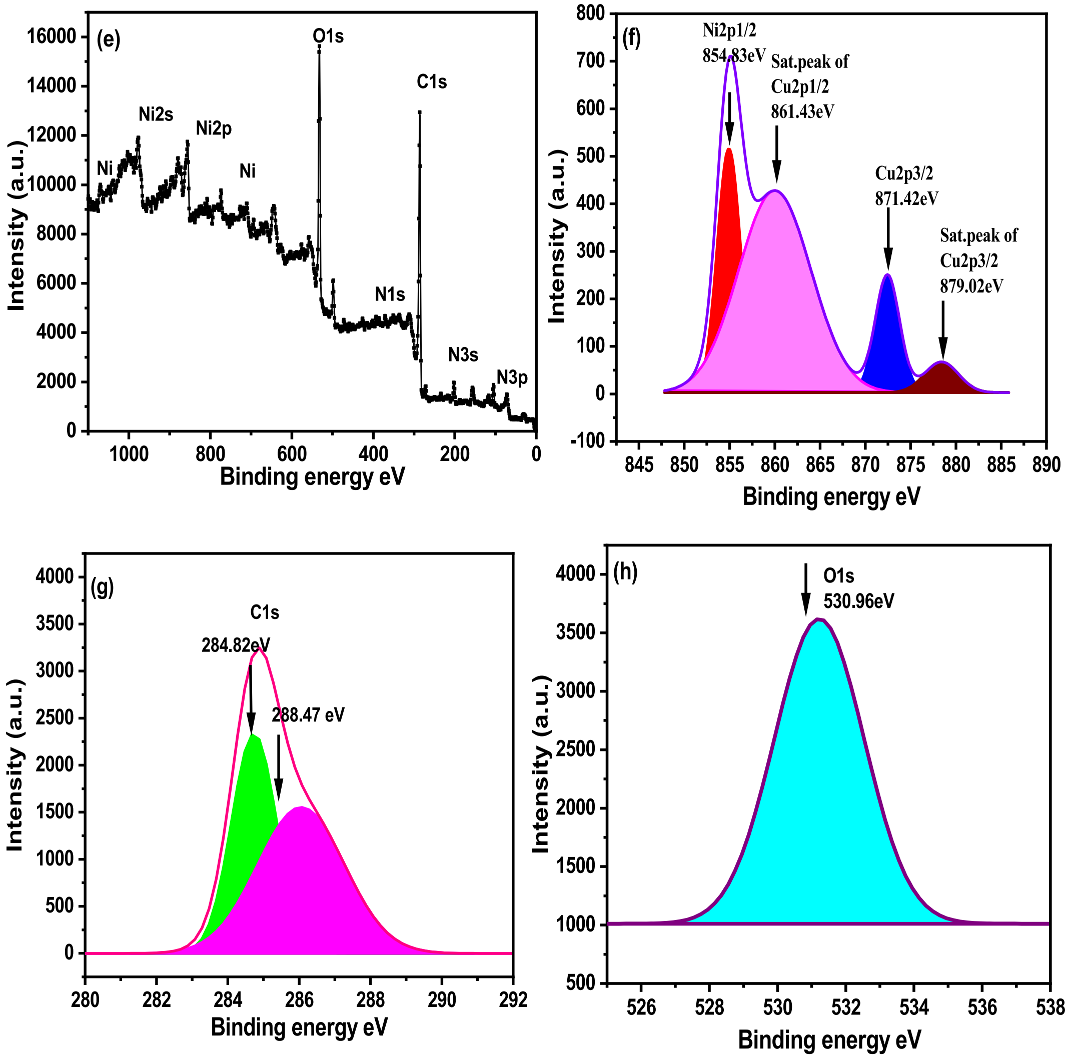

Fig. 5. (*continued*).

Cis@Ni(bpdc)-MOF. The first drop in mass of 8.89 % happened between room temperature and 130 °C. The second mass drop of 10.02 % happened at 130 °C followed by a massive drop in mass of 37.17 % at 340 °C. The final low mass drop of 9.61 % happened between 510 and 580 °C. When the temperature was raised above 580 °C, the mass remained stable with less than 25 % residue left behind. In case of Ni (bpdc)-MOF, it was found to be thermally unstable (Fig. 6(c)) and Cis@Ni(bpdc)-MOF was thermally stable below 440 °C [49]. (See Figs. 7–11.)

3.7. BET analysis

The N_2 sorption isotherms obtained at 77 K using the Brunauer-Emmett- Teller (BET) and Barrett- Joyner-Halenda (BJH) characterization procedures were utilized to assess the samples' surface area, pore size and volume. Cu(bpdc)-MOF and Ni(bpdc)-MOF exhibit type IV isotherms, which are typical of mesoporous materials, on their isotherm curves. The pore size of Cu(bpdc)-MOF and Ni(bpdc)-MOF is 1.916 nm and 1.671 nm whereas the pore size of Cis@Cu(bpdc) and Ni(bpdc)-MOF is reduced to 1.684 nm and 1.417 nm. Similarly, the pore volume of Cu(bpdc)-MOF and Ni(bpdc)-MOF at 0.295cm^3/g and 0.265cm^3/g was reduced to 0.142cm^3/g and 0.108cm^3/g for Cis@Cu (bpdc)-MOF and Cis@Ni(bpdc)-MOF. The obtained results of a decrease in the pore size, volume and surface area show that the cisplatin is encapsulated inside Cu(bpdc)-MOF and Ni(bpdc)-MOF [50,51].

3.8. Photocatalytic activity

The UV–Vis spectra of congo red dye displayed a peak at 498 nm in the nonappearance of Cu(bpdc) and Ni(bpdc)-based MOFs. Dye molecules are generally stable under light irradiation and display resistance to degradation maintaining their absorption intensity without the catalysts. The as-synthesized materials were semiconductors and showed good photocatalytic activity under UV–Visible light irradiation. Upon adding 0.005 g of Cu(bpdc)-MOF and on long exposure to time under UV–Visible light, the intensity of the characteristic peaks of congo red at 498 nm decreased suddenly with no emergence of additional peaks at different time intervals. The red colour of the solution completely disappeared with a degradation efficiency of 99 % after 140mins of irradiation. On the other hand, on adding 0.005 g of Ni(bpdc)-MOF as a catalyst, the complete degradation of congo red is observed after 160mins with 97 % degradation efficiency, indicating that the irradiation process photocatalytic effect destroyed the chromophoric structure of the congo red. The obtained results well matched with the previous reports [52–57]. Ahodashti et al. documented the degradation capacity of the synthesized CF-AgNPs when exposed to UV irradiation, achieving approximately 86.7 % and 81.3 % degradation of basic blue 9 and Eriochrome black T contaminants, respectively, after 110 min [58]. Ahodashi et al. developed $MnFe_2O_4@SiO_2@Au$ magnetic

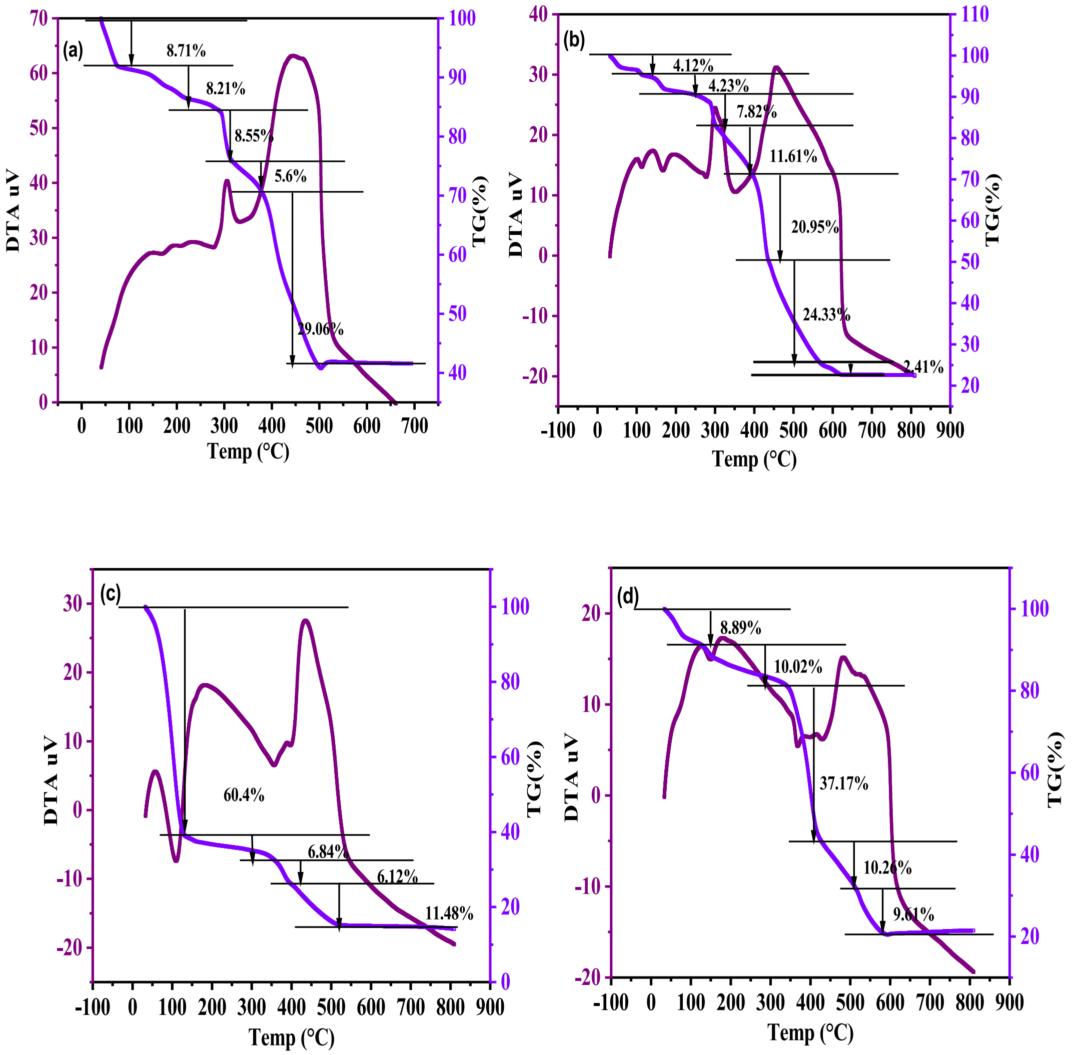

Fig. 6. TGA of (a) Cu(bpdc)-MOF (b) Cis@Cu(bpdc)-MOF (c) Ni(bpdc)-MOF.

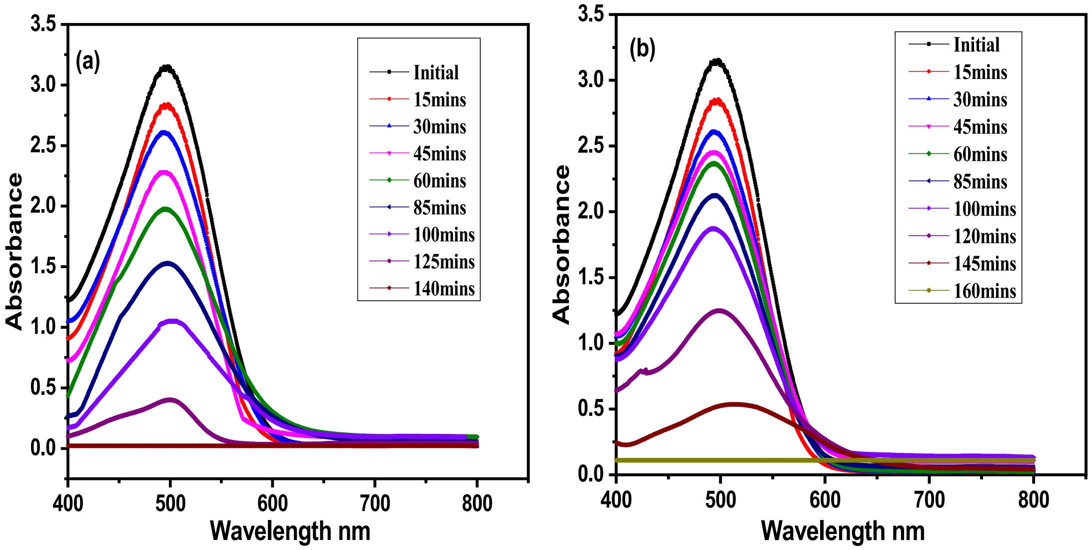

Fig. 7. Photocatalytic degradation of congo red by (a) Cu(bpdc)-MOF (b) Ni(bpdc)-MOF. (For interpretation of the references to colour in this figure legend, the reader is referred to the web version of this article.)

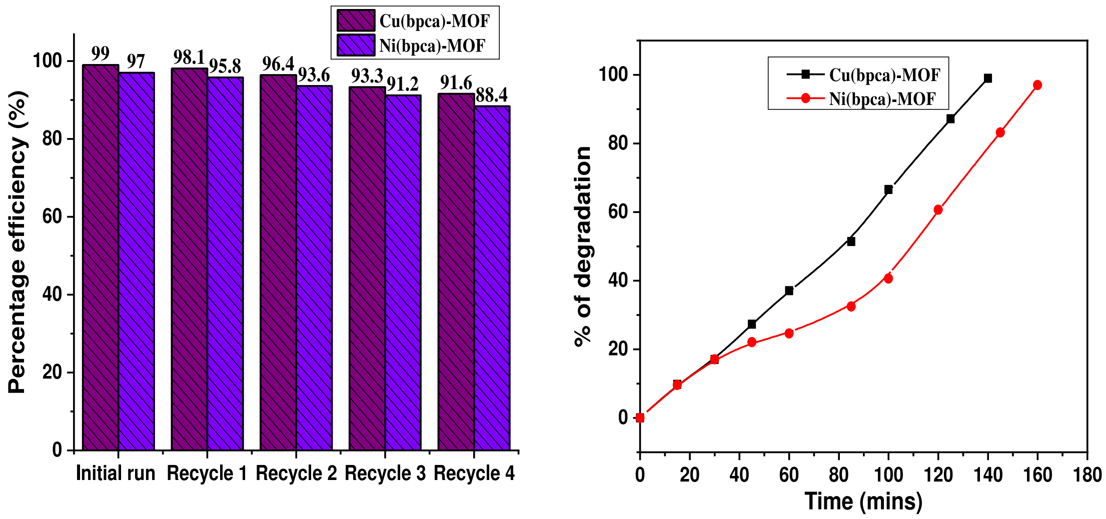

Fig. 8. Recyclability and % of degradation of Cu(bpdc)-MOF and Ni(bpdc)-MOF.

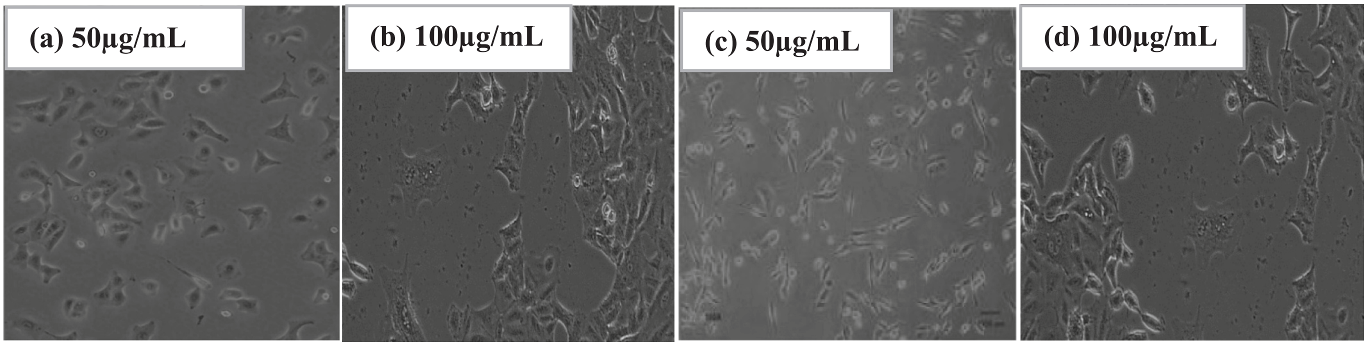

Fig. 9. MDA-MB-231 cell line treated with various concentrations of Cis@Cu@(bpdc)-MOF (a&b) and Cis@Ni(bpdc)-MOF (c&d).

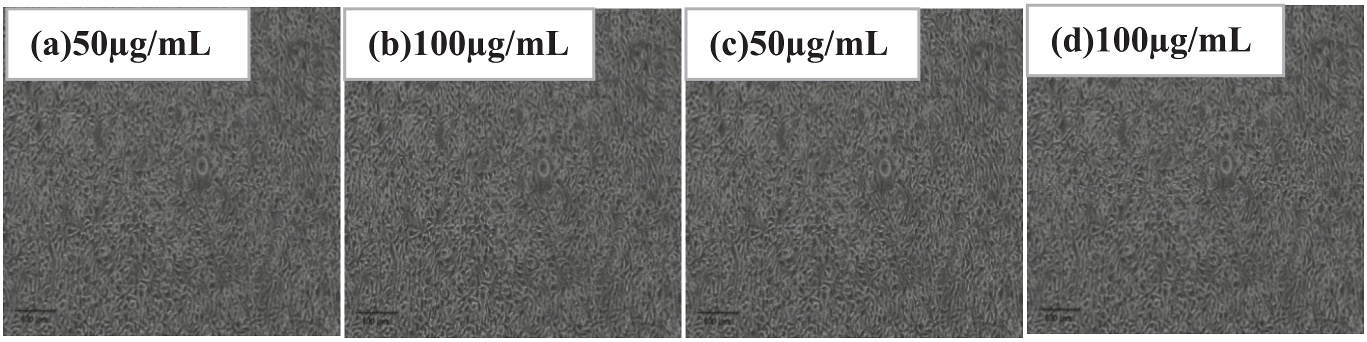

Fig. 10. L-929 cell line treated with various concentrations of Cis@Cu@(bpdc)-MOF (a&b) and Cis@Ni(bpdc)-MOF (c&d).

nanocomposites using glucose, sucrose, and PVA as capping agents, along with *C. pentagyna* and *C. microphylla* serving as reducing agents. The degradation rates of 2-NPH, ER, MV, RhB and EBT under UV irradiation were recorded at 84.3 %, 80.5 %, 87.2 %, 91.2 % and 95.7 %, respectively, while the rates under visible light irradiation were 53.7 %, 49.1 %, 57.9 %, 61.6 % and 64.8 %. After 100 min under UV light, the best degradation of cationic dyes is 87.2 %, whereas the degradation of anionic dyes is over 90 % [59].

Using the following formula, the percentage of Congo red deterioration is determined: % of degradation = $A_0 - A_t / A_0$ x 100.

Where A_0 signifies the absorbance at time $t = 0$ and A_t signifies the absorbance after time t of treatment. A_0 and A_t are recorded at λ_{max} of dye.

3.9. Mechanism of photocatalytic degradation

When organic pollutants undergo photocatalytic treatment, their poisonous byproducts are broken down or changed into harmless forms, allowing for the removal of the pollutants without danger. On exposure to light with energy greater than or equal to its bandgap, photons are absorbed by a semiconductor photocatalyst and it excites the electrons in the valence band, moving them to the conduction band and leaving the valence band with holes or positive charge carriers. The excited holes and electrons are highly reactive and can perform redox reaction on the surface of the photocatalyst. The electron in the conduction band reduce oxygen molecules producing superoxide radicals and the holes in the valence band oxidize hydroxide ions or water molecules producing

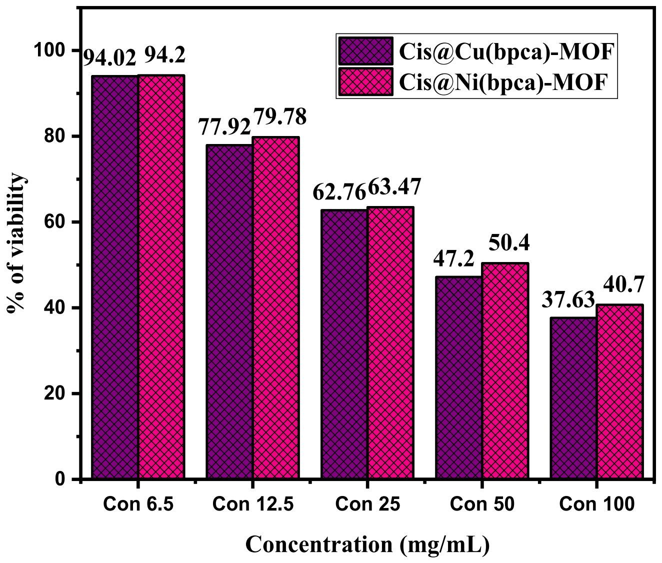

Fig. 11. Graphical representation of concentrations vs % of viability.

hydroxyl radicals. The generated radicals are reactive oxygen species (ROS) that are highly reactive and can decompose the organic pollutants into smaller and less harmful molecules such as CO_2 and H_2O. For trapping reactive oxygen species $^{\bullet}OH$, O_2^{-},h^{+}, e^{-}, scavengers like isopropanol, p-benzoquinone, EDTA and silver nitrate are added to the four identical photocatalytic reaction systems individually and their photocatalytic performance is measured. The degradation significantly decreased with each scavenger which confirmed that the reactive oxygen species played a crucial role in dye degradation.

M(bpdc)-MOF + hυ (M(bpdc)-MOF)* + e^{-} + h^{+} (M = Cu & Ni).
$h^{+} + H_2O\ ^{\bullet}OH + H^{+}$.
$h^{+} + OH^{-}\ ^{\bullet}OH$.
$^{\bullet}OH$+ Dye Degradation product.
$e^{-} + O_2\ ^{\bullet}O_2^{-}$.
$^{\bullet}OH$ + congo red dye Degradation product.
$^{\bullet}O_2^{-}$ + congo red dye Degradation products.

3.10. Recyclability test

The reusability of catalysts is a critical consideration in heterogeneous catalysis applications. Following the experiment, the Cu(bpdc)-MOF and Ni(bpdc)-MOF catalysts were gathered via centrifugation, washed thrice with water and ethanol to eliminate congo red completely and subsequently dried at 100 °C for 5 h before being reused. Despite a slight decrease in photocatalytic degradation efficiency after four cycles, from 99 % to 91 % for Cu(bpdc)-MOF and from 97 % to 88 % for Ni (bpdc)-MOF, these catalysts demonstrated outstanding recyclability and stability under the tested conditions. This suggests that Cu(bpdc)-MOF and Ni(bpdc)-MOF hold promise as potential catalysts for treating organic pollutants in aqueous solutions.

4. Antiproliferative evaluation of Cis@Cu(bpdc)-MOF and Cis@Ni(bpdc)-MOF on MDA-MB-231 by MTT assay method

The assessment of the cytotoxic effects of cisplatin encapsulated within Cu(bpdc)-MOF and Ni(bpdc)-based MOF is conducted through the measurement of cell survival utilizing an MTT (3-(4,5,-dimethylthiazol-2-yl)-2,5-diphenyltetrazolium bromide) assay, which serves to evaluate the mitochondrial functionality of the cells. For an entire day of inhibition, each cultured 96-well plate housing both viable and non-viable cells of the specific cancerous MDA-MB-231 is reserved. The chosen cell lines are tested for their capability to prevent MDA-MB-231 expansion by gradually diluting different doses of Cis@Cu(bpdc)-MOF and Cis@Ni(bpdc)-MOF two times. Cis@Cu(bpdc)-MOF, Cis@Ni (bpdc)-MOF and the untreated control well plates on the 96-well tissue culture cell plate are combined with the reconstituted MTT solution in phosphate buffer solution. The plates are then incubated for many hours at 37 °C with 5 % CO_2 humidity.

The tetrazolium ring in MTT is broken down in active mitochondria to produce the formazan product, a process that can only take place in living cells. Since the purple formazan crystal is insoluble in water, the formazan crystals are dissolved in DMSO. After the liquid supernatant is removed, the dissolved formazan crystals are measured at 570 nm using spectrophotometry. The proportion of living cells is computed from the triplicate responses performed at different concentrations, and the total count is determined by the formazan solution.

$$Percentageofcellularviability = \frac{Averageabsorbanceoftreated}{\text{Average absorbance of control}}\ ^{x}\,100$$

4.1. Antiproliferative evaluation of Cis@cu(bpdc)-MOF against MDA-MB-231

The toxicological effects of Cu(bpdc)-MOF and Cis@Cu(bpdc)-MOF are assessed on MDA-MB-231 breast cancer cells over a duration of 24 h. Samples with varying concentrations of 6.25, 12.5, 25, 50 and 100 μg/mL are meticulously prepared and subsequently evaluated against the cultured cell walls. Following a 24-h exposure to MDA-MB-231 cells, the viability of these cells subjected to Cis@Cu(bpdc)-MOF at concentrations of 6.25 μg/mL and 12.5 μg/mL decreased from the baseline to 94.02 % and 77.92 %, respectively. Furthermore, the cellular viability in MDA-MB-231 cells fell to around 62.76 %, 47.2 % and 37.63 % when the concentration is increased to 25, 50 and 100 μg/mL. The cytotoxicity of Cis@Cu(bpdc)-MOF is significantly greater than the toxic effects of Cu (bpdc)-MOF which showed a cellular viability of 74 % at the highest concentration of 100 μg/mL. Because cisplatin creates DNA adducts, which disrupt DNA replication and transcription and cause cancer cells to apoptose, it has a cytotoxic impact, reducing cell viability. Further, the Cu(bpdc)-MOF's released copper ions aided cytotoxicity by producing reactive oxygen species (ROS), which in turn damage cancer cell DNA. On a typical day, cancer cells experience oxidative stress, which is characterized by high metabolic activity and increased quantities of reactive oxygen species (ROS) compared to normal cells. In addition, cancer cells are unable to repair the DNA damage caused by cisplatin because copper ions hinder certain DNA repair enzymes. The synergistic interaction between cisplatin and Cu(bpdc)-MOF causes morphological disruption as a result of the combined effects of ROS produced by the compound and DNA damage induced by cisplatin. The IC_{50} of Cis@Cu (bpdc)-MOF loaded with 31.53 % of cisplatin is 55 μg/mL with the percentage of growth inhibition from 5.98 % to 62.37 %. The obtained results suited with the previously reported ones [60–62]. According to Tanay et al., Doxorubicin-loaded Gd-based MOFs demonstrated similar outcomes. By using the MTT test on the U 937 leukaemia cancer cell line, we were able to confirm that 5 wt% DOX loaded MG-Gd-pDBI has anticancer activity. At the two distinct doses of 75 and 300 μg/mL, about 50 % and 29 % of viable cells, respectively, were found [63]. By using the MTT test, Kai et al. assessed the anticancer efficacy of CPT-loaded ZIF-8@RGD against HeLa (cancer) and HEK-293 T (normal) cells. Compared to HEK-293 T cellular apoptosis, the CPT@ZIF-8@RGD nanoparticles killed around 75 % of HeLa cells at a concentration of 50 μg/mL (containing 5 μg/mL CPT). Based on these findings, CPT@ZIF-8@RGD nanoparticles have the potential to be a very effective hydrophobic anticancer medication delivery method for precision cancer therapy [64].

4.2. Antiproliferative evaluation of Cis@Ni(bpdc)-MOF against MDA-MB-231

For 24 h, MDA-MB-231 cell is used to assess the toxicities of Ni (bpdc)-MOF and Cis@Ni(bpdc)-MOF. A range of concentrations (6.25, 12.5, 25, 50 and 100 μg/mL) of test samples are generated and subjected to cell wall culture testing. The MDA-MB-231 cells treated with 6.25 μg/mL and 12.5 μg/mL of Cis@Ni(bpdc)-MOF saw a decrease in cellular viability from base level to 94.2 % and 79.78 % after a 24-h treatment period. Furthermore, when the concentration was increased to 25, 50 and 100 μg/mL, the cellular viability in MDA-MB-231 cells decreased to approximately 62 %, 50.4 % and 40.7 %. Cis@Ni(bpdc)-MOF exhibits cytotoxicity that is noticeably greater than Ni(bpdc)-MOF's toxic effects. In the case of Ni(bpdc)-MOF, the cellular viability in MDA-MB-231 line is 79 %. The reduction in cell viability is brought on by the cytotoxic impact of cisplatin, which creates DNA adducts that obstruct transcription and DNA replication and ultimately cause cancer cells to undergo apoptosis. Additionally, the nickel ion from Ni(bpdc)-MOF produces reactive oxygen species (ROS), which harm cancer cells' DNA and contribute to cytotoxicity. In contrast to non-tumorous cells, cancer cells typically experience oxidative stress, which is typified by high amounts of ROS and high metabolic activity. Due to the synergistic interaction between cisplatin and the ROS produced by Ni(bpdc)-MOF, morphological disruption results from the combined effect of both substances. The IC_{50} of Cis@Ni(bpdc)-MOF loaded with 27.17 % of cisplatin is 62.15 μg/ml with the percentage of growth inhibition from 5.8 % to 59.3 %. The combined action of cisplatin and Ni(bpdc)-MOF results in increased cytotoxicity of Cis@Ni(bpdc)-MOF. The obtained results suited with the previously reported ones [65–68]. Su et al. synthesized one-pot encapsulated UiO-66@AgNCs@Apt@DOX and evaluated their anticancer activity against breast cancer MCF-7 and normal L929 cell lines by MTT assay. At a DOX concentration of 10 μg/mL killed about 80.3 % of MCF-7 cells, but only 54.9 % of L929 cells died under the same circumstances [69]. Liang et al. reported the cytotoxicity of Doxorubicin-loaded BSA@ZIF-8 against breast cancer MCF-7 cell line by MTT assay. After 24 h of incubation with concentrations of 0.5 and 1 mg/L, the mitochondrial function fell to 33 and 17 % respectively. Additionally, after 72 h of BSA/DOX@ZIF incubation, the mitochondrial activity in MCF-7 cells decreased to about 10 % at a concentration of 1 mg/L [70]. Alireza et al. revealed the preparation of oxaliplatin-loaded UiO-66-NH_2 and examined its cytotoxicity against CT-26 cells by MTT assay. The test highlighted that no significant cytotoxicity was caused by UiO-66-NH_2 alone but for oxaliplatin-loaded UiO-66-NH_2 the death of the cells was significantly increased [71,72].

4.3. Antiproliferative evaluation of Cis@Cu(bpdc)-MOF and Cis@Ni(bpdc)-MOF against normal L929 cell line

The Cis@Cu(bpdc)-MOF showed no toxicity to normal cells before entering the cancer cells. It is confirmed when the toxicity of Cis@Cu(bpdc)-MOF is tested against the normal L-929 mouse fibroblast cell line. After treatment with L-929 cells for 24 h, the cellular viability in L-929 cells tested with Cis@Cu(bpdc)-MOF at a concentration of 6.25, 12.5, 25, 50 and 100 μg/mL showed cellular viability of 98.87, 97.51, 96.15, 95.48 and 94.68 % and Cis@Ni(bpdc)-MOF exhibited cellular viability of 98.24, 97.66, 96.37, 95.32 and 93.68 %, indicating no toxicity was noticed in normal cells. L929 cells exhibit lower uptake efficiency for Cis@Cu(bpdc)-MOF and Cis@Ni(bpdc)-MOF and do not internalize the MOF particles as efficiently as cancer cells, reducing their exposure to cisplatin. The Cu(bpdc)-MOF and Ni(bpdc)-MOF are biocompatible, therefore the copper ions and the organic ligand (biphenyl dicarboxylate) in the MOF structure are unlikely to cause significant toxicity at low concentrations. Normal cells, like L929, can neutralize reactive oxygen species (ROS) and reduce toxicity because they have higher antioxidant systems.

5. Conclusion

In conclusion, the Cu(bpdc)-MOF and Ni(bpdc)-MOF were successfully synthesized using a hydrothermal approach and characterized using various advanced techniques, including XRD, SEM-EDX, FT-IR, UV–Vis DRS, XPS, TGA and N_2 sorption analysis. The photocatalytic properties of these MOFs were evaluated through the degradation of Congo Red dye under visible light irradiation, achieving degradation efficiencies of 99 % and 97 % for Cu(bpdc)-MOF and Ni(bpdc)-MOF, respectively. The complete degradation of Congo Red (2 mg/L) was achieved within 145 min for Cu(bpdc)-MOF and 160 min for Ni(bpdc)-MOF. Importantly, both catalysts demonstrated excellent reusability and stability over multiple cycles, which is critical for minimizing operational costs and avoiding secondary pollution in wastewater treatment applications. These findings highlight the potential of Cu(bpdc)-MOF and Ni(bpdc)-MOF as robust photocatalysts for environmental remediation. Additionally, a simple impregnation method was employed to encapsulate cisplatin within the Cu(bpdc)-MOF and Ni(bpdc)-MOF frameworks, resulting in high cisplatin loading and the development of effective drug delivery systems. Both Cis@Cu(bpdc)-MOF and Cis@Ni(bpdc)-MOF demonstrated excellent biocompatibility and stability, alongside significant therapeutic efficacy against the breast cancer MDA-MB-231 cell line. The in vitro cytotoxicity studies revealed IC_{50} values of 55.78 μg/mL and 62.15 μg/mL for Cis@Cu(bpdc)-MOF and Cis@Ni(bpdc)-MOF, respectively, underscoring their potential for cancer treatment. This study bridges the fields of environmental science and biomedicine by demonstrating the dual functionality of Cu(bpdc)-MOF and Ni(bpdc)-MOF as photocatalysts for pollutant degradation and as efficient drug delivery systems. These multifunctional materials address global challenges such as wastewater treatment and targeted cancer therapy, providing a foundation for future innovations in sustainable and versatile material design.

Funding declaration

The authors have no funding to report.

Declaration of competing interest

The authors declare that they have no known competing financial interests or personal relationships that could have appeared to influence the work reported in this paper.

Data availability

Data will be made available on request.

References

[1] W. Lu, Z. Wei, Z.Y. Gu, T.F. Liu, J. Park, J. Park, J. Tian, M. Zhang, Q. Zhang, T. Gentle, M. Bosch, H.C. Zhou, Tuning the structure and function of metal-organic frameworks via linker design, Chem. Soc. Rev. 43 (2014) 5561–5593, https://doi.org/10.1039/C4CS00003J.

[2] K. Jiang, L. Zhang, Q. Hu, Y. Yang, W. Lin, Y. Cui, Y. Yang, G. Qian, A biocompatible Ti-based metal-organic framework for pH-responsive drug delivery, Mater. Lett. 225 (2018) 142–144, https://doi.org/10.1016/j.matlet.2018.05.006.

[3] K. Akhbari, A. Morsali, Needle-like hematite nano-structure prepared by directed thermolysis of MIL-53 nano-structure with enhanced methane storage capacity, Mater. Lett. 141 (2015) 315–318, https://doi.org/10.1016/j.matlet.2014.11.110.

[4] B. Yu, F. Wang, W. Dong, J. Hou, P. Lu, J. Gong, Self-template synthesis of core-shell ZnO@ZIF-8 nanospheres and the photocatalysis under UV irradiation, Mater. Lett. 156 (2015) 50–53, https://doi.org/10.1016/j.matlet.2015.04.142.

[5] J. Liu, J.X. Hou, J.P. Gao, J.M. Liu, X. Jing, L.J. Li, J.L. Du, Stable cd(II)-MOF as a fluorescent sensor for efficient detection of uranyl ions, Mater. Lett. 241 (2019) 184–186.

[6] A. Inyinbor Adejumoke, O. Adebesin Babatunde, P. Oluyori Abimbola, A. Adelani Akande, Tabitha, O. Dada Adewumi, A. Oreofe Toyin, water challenges of an urbanizing, World (2018) 33–53, https://doi.org/10.5772/intechopen.68339.

[7] D. Rawat, V. Mishra, R.S. Sharma, Detoxification of azo dyes in the context of environmental processes, Chemosphere 155 (2016) 591–605, https://doi.org/10.1016/J.CHEMOSPHERE.2016.04.068.

[8] B.J. Bruschweiler, C. Merlot, Azo dyes in clothing textiles can be cleaved into a series of mutagenic aromatic amines which are not regulated yet, Regul. Toxicol. Pharmacol. 88 (2017) 214–226, https://doi.org/10.1016/J.YRTPH.2017.06.012.

[9] N.A. Travlou, G.Z. Kyzas, N.K. Lazaridis, E.A. Deliyanni, Graphite oxide/chitosan composite for reactive dye removal, Chem Eng J. 217 (2013) 256–265, https://doi.org/10.1016/j.cej.2012.12.008.

[10] Y.S. Woo, M. Rafatullah, A.F.M. Al-Karkhi, T.J. Tow, Removal of terasil red R dye by using Fenton oxidation: a statistical analysis, desalination, Water Treat. 52 (2014) 4583–4591, https://doi.org/10.1080/19443994.2013.804454.

[11] X. Lei, X. Li, Z. Ruan, T. Zhang, F. Pan, Q. Li, D. Xia, J. Fu, Adsorption-photocatalytic degradation of dye pollutant in water by graphite oxide grafted titanate nanotubes, J. Mol. Liq. 256 (2018) 122–131, https://doi.org/10.1016/j.molliq.2018.06.053.

[12] M.R. Gadekar, M.M. Ahammed, Coagulation/flocculation process for dye removal using water treatment residuals: modelling through artificial neural networks, desalination, Water Treat. 57 (2016) 26392–26400, https://doi.org/10.1080/19443994.2016.1165150.

[13] I.M.C. Goncalves, A. Gomes, R. Bras, M.I.A. Ferra, M.T.P. Amorim, R. Porter, Biological treatment of effluent containing textile dyes coloration, Techonolgy 116 (2000) 393–397, https://doi.org/10.1111/j.1478-4408.2000.tb00016.x.

[14] C. Tamaraiselvan, M. Noel, Membrane processes for dye wastewater treatment: recent progress in fouling control critical, Rev. Environ. Sci. Technol. 45 (2015) 1007–1040, https://doi.org/10.1080/10643389.2014.900242.

[15] M.J. Nurhidayatullaili, B. Samira, B.A.H. Sharifah, Recent advances in heterogeneous photocatalytic decolorization of synthetic dyes, Sci. World J. 3383 (2014) 692307, https://doi.org/10.1155/2014/692307.

[16] C.C. Wang, J.R. Li, X.L. Lv, Y.Q. Zhang, G. Guo, Photocatalytic organic pollutants degradation in metal-organic frameworks, Energy Environ. Sci. 7 (2014) 2831–2867, https://doi.org/10.1039/C4EE01299B.

[17] M.R. Hoffmann, S.T. Martin, W. Choi, D.W. Bahnemann, Environmental applications of semiconductor photocatalysis, Chem. Rev. 95 (1995) 68–96, https://doi.org/10.1021/cr00033a004.

[18] T.L. Thompson, J.T. Yates, Surface science studies of the photoactivation of TiO2- a new photochemical processes, Chem. Rev. 106 (2016) 4428, https://doi.org/10.1021/cr050172k.

[19] A. Mills, S. Le Hunte, An overview of semiconductor photocatalysis, J. Photochem. Photobiol. A Chem. 108 (1997) 1–35, https://doi.org/10.1016/S1010-6030(97)00118-4.

[20] K. Ayoub, E.D. Van Hullebusch, M. Cassir, A. Bermond, Application of advanced oxidation processes for TNT removal: a review, J. Hazard. Mater. 178 (2010) 10–28, https://doi.org/10.1016/j.jhazmat.2010.02.042.

[21] T. Zhang, W. Lin, Metal-organic frameworks for artificial photosynthesis and photocatalysis, Chem. Soc. Rev. 43 (2014) 5982–5993, https://doi.org/10.1039/c4cs00103f.

[22] P. Mahata, G. Madras, S. Natarajan, Novel photocatalysts for the decomposition of organic dyes based on metal-organic framework compounds, J. Phys. Chem. B 110 (2006) 13759–13768, https://doi.org/10.1021/jp0622381.

[23] Q. Xia, X. Yu, H. Zhao, S. Wang, H. Wang, Z. Guo, H. Xing, Syntheses of novel lanthanide metal-organic frameworks for highly efficient visible-light driven dye degradation, Cryst. Growth Des. 17 (2017) 4189–4195, https://doi.org/10.1021/acs.cgd.7b00504.

[24] R.L. Siegel, K.D. Miller, N.S. Wagle, A. Jemal, Cancer statistics, CA-Cancer J. Clin. 65 (2015) 11–30, https://doi.org/10.3322/caac.21763.

[25] P. Masso-Welch, S.G. Berlingeri, N.D. King-Lyons, L. Mandell, J. Hu, C.J. Greene, M. Federowicz, P. Cao, T.D. Connell, Y. Heakal, LT-IIc, a bacterial type II heat-labile enterotoxin, induces specific lethality in triple-negative breast cancer cells by modulation of autophagy and induction of apoptosis and necroptosis, Int. J. Mol. Sci. 20 (2018) 85, https://doi.org/10.3390/ijms20010085.

[26] W. Zhang, J.H. Mao, W. Zhu, A.K. Jain, K. Liu, J.B. Brown, G.H. Karpen, Centromere and kinetochore gene Misexpression predicts Cancer patient survival and response to radiotherapy and chemotherapy, Nat. Commun. 7 (2016) 12619, https://doi.org/10.1038/ncomms12619.

[27] R.A. Petros, J.M. DeSimone, Strategies in the design of nanoparticles for therapeutic applications, Nat. Rev. Drug Discov. 9 (2010) 615–627, https://doi.org/10.1038/nrd2591.

[28] M. Ding, W. Liu, R. Gref, Nanoscale MOFs: from synthesis to drug delivery and theranostics applications, Adv. Drug Deliv. Rev. 190 (2022) 114496, https://doi.org/10.1016/j.addr.2022.114496.

[29] H. Zheng, Y. Zhang, L. Liu, W. Wan, P. Guo, A.M. Nystrom, X. Zou, One-pot synthesis of metal-organic frameworks with encapsulated target molecules and their applications for controlled drug delivery, J. Am. Chem. Soc. 138 (2016) 962–968, https://doi.org/10.1021/jacs.5b11720.

[30] Y. Yang, Q. Hu, Q. Zhang, K. Jiang, W. Lin, Y. Yang, Y. Cui, G.A. Qian, Large capacity cationic metal-organic framework Nanocarrier for physiological pH-responsive drug delivery, Mol. Pharm. 13 (2016) 2782–2786, https://doi.org/10.1021/acs.molpharmaceut.6b00374.

[31] W. Zhang, H. Yin, Z. Yu, X. Jia, J. Liang, G. Li, Y. Li, K, Wang, facile synthesis of 4,4′-biphenyl dicarboxylic acid-based nickel metal-organic frameworks with a tunable pore size towards high-performance supercapacitors, Nanomaterials 12 (2021) 2062, https://doi.org/10.3390/nano12122062.

[32] C. Gong, H. Guo, X. Zeng, H. Xu, Q. Zeng, J. Zhang, J. Xie, Flexible and rigid dicarboxylic acids enable the assembly of achiral and chiral 3D co(II) metal-organic frameworks, Dalton Trans. 47 (2018) 6917–6923, https://doi.org/10.1039/C8DT00600H.

[33] W. Starosta, B. Sartowska, K. Lyczko, J. Maurin, A. Pawlukojc, L. Walis, M. Buczkowski, A method for production of nano MOF and preliminary characterization by selected analytical techniques, Nukleonika 57 (2012) 581–583.

[34] R. Ardeleanu, A. Dascalu, S. Shova, A. Nicolescu, I. Rosca, B. Bratanovici, V. Lozan, G. Roman, 4′-(2H-tetrazol-5-yl)-[1,1′-biphenyl]-4-carboxylic acid: synthetic approaches, single crystal X-ray structures and antimicrobial activity of intermediates, J. Mol. Struct. 1173 (2018) 63–71, https://doi.org/10.1016/j.molstruc.2018.06.086.

[35] X. Wang, Q. Li, N. Yang, F. He, J. Chu, M. Gong, B. Wu, R. Zhang, S. Xiong, Hydrothermal synthesis of NiCo-based bimetal-organic frameworks as electrode materials for supercapacitors, J. Solid State Chem. 270 (2019) 370–378, https://doi.org/10.1016/j.jssc.2018.11.038.

[36] D.K. Singha, P. Majee, S.K. Mondal, P. Mahata, P., A luminescent cadmium-based MOF as selective and sensitive iodide sensor in aqueous medium, J. Photochem. Photobiol. A Chem. 356 (2018) 389–396, https://doi.org/10.1016/j.jphotochem.2018.01.024.

[37] X. Wang, M. Kumar Ghosh, P. Zhuang, X. Zhang, Y. Wu, M. Muddassir, T. Kumar Ghorai, D. Srivastava, S. Srivastava, A. Kumar, 4′-((4-cyanobenzyl)oxy)-[1,1′-biphenyl] -4-carboxylic acid-based cd(II), co(II), Mn(II) and Ni(II) coordination polymers as photocatalyst for nitrofurazone degradation, Inorg. Chim. Acta 562 (2024) 121892, https://doi.org/10.1016/j.ica.2023.121892.

[38] H.R. Zhang, X.Q. Kang, J.Z. Gu, Synthesis of coordination compounds with 4′-(carboxymethoxy)-[1,1′-biphenyl]-4-carboxylate ligand and their catalytic activities towards the Knoevenagel condensation and cyanosilylation reactions, J. Saudi Chem. Soc. 28 (2024) 101817, https://doi.org/10.1016/j.jscs.2024.101817.

[39] H. Yang, S. Orefuwa, A. Goudy, Study of mechanochemical synthesis in the formation of the metal-organic framework $Cu_3(BTC)_2$ for hydrogen storage, Microporous Mesoporous Mater. 143 (2011) 37–45, https://doi.org/10.1016/j.micromeso.2011.02.003.

[40] F. He, N. Yang, K. Li, X. Wang, S. Cong, L. Zhang, S. Xiong, A. Zhou, Hydrothermal synthesis of Ni-based metal-organic frameworks/graphene oxide composites as supercapacitor electrode materials, J. Mater. Res. 35 (2020) 1439–1450, https://doi.org/10.1557/jmr.2020.93.

[41] M. Ghaferi, S. Amari, B.V. Mohrir, A. Raza, H.E. Shahmabadi, S.E. Alavi, S, preparation, characterization, and evaluation of cisplatin-loaded Polybutylcyanoacrylate nanoparticles with improved in vitro and in vivo anticancer activities, Pharmaceuticals 13 (2020), https://doi.org/10.3390/ph13030044.

[42] A.H. Shah, Z.U. Abideen, S. Maqsood, F. Rashid, R. Ullah, A.U. Rehman, M. Dildar, M. Ahmad, K. Ullah, M.N. Rafi, F. Teng, Porous cu-based metal-organic framework (cu-MOF) for highly selective adsorption of organic pollutants, J. Solid-State Chem. 322 (2023) 123935, https://doi.org/10.1016/j.jssc.2023.123935.

[43] J. Xu, C. Yang, Y. Xue, C. Wang, J. Cao, Z. Chen, Facile synthesis of novel metal-organic nickel hydroxide nanorods for high performance supercapacitor, Electrochim. Acta 211 (2016) 595–602, https://doi.org/10.1016/j.electacta.2016.06.090.

[44] A. Kojtari, H.F. Ji, Metal-organic framework micro/nanopillars of cu(BTC).3H2O and Zn(ADC), DMSO Nanomater. 5 (2015) 565–567, https://doi.org/10.3390/nano5020565.

[45] K. Ma, C. Bi, X. Zhang, Z. Zong, C. Fan, C. Xu, Y.H. Fan, Synthesis of two different Ni(II) coordination polymers by introduction of carboxylic acid ligands: crystal structure and photocatalytic properties, Inorg. Chim. Acta 494 (2019) 91–97, https://doi.org/10.1016/j.ica.2019.04.042.

[46] C. Magallanes, B.M. Aguirre, G.A. Gonzalez, L.P. Mendez De Leo, Interaction of aqueous cu(II) with carboxylic acid and alcohol terminated self-assembled monolayers: surface and interfacial characterization, Surf. Sci. 692 (2020) 121529, https://doi.org/10.1016/j.susc.2019.121529.

[47] H. Yan, J. Bai, J. Wang, X. Zhang, B. Wang, Q. Liu, L. Liu, Graphene homogeneously anchored with Ni(OH)2 nanoparticles as advanced supercapacitor electrodes, Cryst. Eng. Comm. 15 (2013) 10007–10015, https://doi.org/10.1039/C3CE41361F.

[48] Y. Shiraishi, H. Tomita, K. Fujiki, H. Hirai, One-step synthesis of 4,4′-biphenyldicarboxylic acid from biphenyl using cyclodextrin as catalyst, React. Funct. Polym. 36 (1998) 99–102, https://doi.org/10.1016/S1381-5148(97)00096-5.

[49] H. Salam, H.N. Nassar, A. Khidr, T. Zaki, Antimicrobial activities of green synthesized ag nanoparticles@Ni-MOF nanosheets, J. Inorg. Organomet. P. 28 (2018) 2791–2798, https://doi.org/10.1007/s10904-018-0950-4.

[50] R. Du, Y. Wu, Y. Yang, T. Zhai, T. Zhou, Q. Shang, L. Zhu, C. Shang, Z. Guo, Porosity engineering of MOF-based materials for electrochemical energy storage, Adv. Energy Mater. 11 (2021) 2100154, https://doi.org/10.1002/aenm.202100154.

[51] D.Y. Lee, D.V. Shinde, E.K. Kim, W. Lee, I.W. Oh, N.K. Shrestha, J.K. Lee, S.H. Han, Supercapacitive property of metal-organic frameworks with different pore dimensions and morphology, Microporous Mesoporous Mater. 171 (2013) 5357, https://doi.org/10.1016/j.micromeso.2012.12.039.

[52] M.A. Ebrahimzadeh, A. Naghizadeh, S. Mohammadi-Aghdam, H. Khojasteh, S. M. Ghoreishi, S. Mortazavi-Derazkola, Enhanced catalytic and antibacterial efficiency of biosynthesized Convolvulus fruticosus extract capped gold nanoparticles (CFE@AuNPs), J. Photochem. Photobiol. B Biol. 209 (2020) 111949, https://doi.org/10.1016/j.jphotobiol.2020.111949.

[53] M. Shirzadi-Ahodashti, Z.M. Mizwari, Z. Hashemi, S. Rajabalipour, S.M. Ghoreishi, S. Mortazavi-Derazkola, M.A. Ebrahimzadeh, Discovery of high antibacterial and catalytic activities of biosynthesized silver nanoparticles using C. Fruticosus (CF-AgNPs) against multi-drug resistant clinical strains and hazardous pollutants, Environ. Technol. Innov. 23 (2021) 101607, https://doi.org/10.1016/j.eti.2021.101607.

[54] S.M. Ghoreishi, S. Mortazavi-Derazkola, Eco-friendly synthesis of gold nanoparticles via tangerine peel extract: unveiling their multifaceted biological

and catalytic potentials, Heliyon 11 (2025) e40104, https://doi.org/10.1016/j.heliyon.2024.e40104.

[55] K. Khormali, Z.M. Mizwari, S. Masoumeh Ghoreishi, S. Mortazavi-Derazkola, B. Khezri, Novel Dy_2O_3/ZnO-au ternary nanocomposites: green synthesis using pomegranate fruit extract, characterization and their photocatalytic and antibacterial properties, Bioorg. Chem. 115 (2021) 105204, https://doi.org/10.1016/j.bioorg.2021.105204.

[56] R. Xiang, C. Zhou, Y. Liu, T. Qin, D. Li, X. Dong, M. Muddassir, A. Zhong, A new type co(II)-based photocatalyst for the nitrofurantoin antibiotic degradation, J. Mol. Struct. 1312 (2024) 138501, https://doi.org/10.1016/j.molstruc.2024.138501.

[57] Y. Wu, X. He, X. Wang, J. Xv, M. Muddassir, I.A. Ansari, A. Zhong, Synergistic efficacy unleashed: co/Ni-based catalysts as a versatile powerhouse for photocatalytic degradation of ornidazole, Inorg. Chim. Acta 568 (2024) 122115, https://doi.org/10.1016/j.ica.2024.122115.

[58] S.M. Ghoreishi, Facile synthesis and characterization of $CaWO_4$ nanoparticles using a new Schiff base as capping agent: enhanced photocatalytic degradation of methyl orange, J. Mater. Sci. Mater. Electron. 28 (2017) 14833–14838, https://doi.org/10.1007/s10854-017-7354-z.

[59] M. Shirzadi-Ahodashti, M.A. Ebrahimzadeh, S.M. Ghoreishi, A. Naghizadeh, S. Mortazavi-Derazkola, Facile and eco-benign synthesis of a novel $MnFe_2O_4$@SiO_2@au magnetic nanocomposite with antibacterial properties and enhanced photocatalytic activity under UV and visible-light irradiations, Appl. Organomet. Chem. 34 (2020) e5614, https://doi.org/10.1002/aoc.5614.

[60] Z. Kiani, S. Mirjalili, K. Heydaryan, P. Mohammadparast, H. Aramjoo, F. Bahraini, A. Yousefinia, M. Torabi, S.M. Ghoreishi, M. Fattahi, S. Mortazavi-Derazkola, Harmonizing nature and nanotechnology: Phytoextract-mediated synthesis of ag-doped ZnO nanoparticles using Lavandula stoechas extract for environmental and biomedical applications, J. Drug Delivery Sci. Technol. 96 (2024) 105708, https://doi.org/10.1016/j.jddst.2024.105708.

[61] A. Naghizadeh, Z.M. Mizwari, S.M. Ghoreishi, S. Lashgari, S. Mortazavi-Derazkola, B. Rezaie, Biogenic and eco-benign synthesis of silver nanoparticles using jujube core extract and its performance in catalytic and pharmaceutical applications: removal of industrial contaminants and in-vitro antibacterial and anticancer activities, Environ. Technol. Innov. 23 (2021) 101560, https://doi.org/10.1016/j.eti.2021.101560.

[62] H. Aidi, D. Yuhang, S. Yumeng, P. Zhixin, L. Sitong, X. Shenao, Z. Xinshuo, M. Lufang, L. Baozhong, W. Haixia, Z. Zhan, CuS/co-ferrocene-MOF nanocomposites for Photothermally enhanced Chemodynamic antibacterial therapy, ACS Appl. Nano Mater 7 (2024) 10998–11007, https://doi.org/10.1021/acsanm.4c02067.

[63] K. Tanay, M. Shouvik, P. Prasun, G. Arunava, D.D. David, B. Rahul, Mechanical downsizing of a gadolinium(III)-based metal-organic framework for anticancer drug delivery, chemistry-a, Eur. J. 20 (2014) 10514–10518, https://doi.org/10.1002/chem.201402244.

[64] K. Dong, Y. Zhang, L. Zhang, Z. Wang, J. Ren, X. Qu, Facile preparation of metal-organic frameworks-based hydrophobic anticancer drug delivery nanoplatform for targeted and enhanced cancer treatment, Talanta 194 (2019) 703–708, https://doi.org/10.1016/j.talanta.2018.10.101.

[65] S. Shaaban, M.S.S. Adam, N.M. El-Metwaly, Novel organoselenium-based N-mealanilic acid and its zinc (II) chelate: catalytic, anticancer, antimicrobial, antioxidant, and computational assessments, J. Mol. Liq. 363 (2022) 119907, https://doi.org/10.1016/j.molliq.2022.119907.

[66] S. Shaaban, A. Zarrouk, D. Vervandier-Fasseur, Y.S. Al-Faiyz, H. El-Sawy, I. Althagafi, P. Andreoletti, M. Cherkaoui-Malki, Cytoprotective organoselenium compounds for oligodendrocytes, Arab. J. Chem. 14 (2021) 103051, https://doi.org/10.1016/j.arabjc.2021.103051.

[67] X. Li, X. Zhao, D. Chu, X. Zhu, B. Xue, H. Chen, Z. Zhou, J. Li, Silver nanoparticle-decorated 2D co-TCPP MOF nanosheets for synergistic photodynamic and silver ion antibacterial, Surfaces and Interfaces. 33 (2022) 102247, https://doi.org/10.1016/j.surfin.2022.102247.

[68] Z. Zhan, W. Tao, H. Tingting, C. Chunhua, Y. Shilong, L. Hai, L. Shuyan, M. Lufang, Z. Meiting, L. Ruizheng, T. Chaoliang, Facile synthesis of 2D Al-TCPP MOF nanosheets for efficient sonodynamic cancer therapy, Mater. Chem. Front. 7 (2023) 1684–1693, https://doi.org/10.1039/D2QM01333A.

[69] F. Su, Q. Jia, Z. Li, M. Wang, L. He, D. Peng, Y. Song, Z. Zhang, S. Fang, Aptamer-templated silver nanoclusters embedded in zirconium metal-organic framework for targeted antitumor drug delivery, Microporous Mesoporous Mater. 275 (2019) 152–162, https://doi.org/10.1016/j.micromeso.2018.08.026.

[70] Z. Liang, Z. Yang, H. Yuan, C. Wang, J. Qi, K. Liu, R. Cao, H. Zheng, A protein@metal-organic framework nanocomposite for pH-triggered anticancer drug delivery, Dalton Trans. 47 (2018) 10223–10228, https://doi.org/10.1039/C8DT01789A.

[71] A. Hashemzadeg, F. Amerizadeh, F. Asgharzadeh, M. Darroudi, A. Avan, S. M. Hassanian, M. Landarani, M. Khazaei, Delivery of oxaliplatin to colorectal cancer cells by folate-targeted UiO-66-NH_2, Toxicol. Appl. Pharmacol. 423 (2021) 115573, https://doi.org/10.1016/j.taap.2021.115573.

[72] J. Hu, Z. Xu, D. Liao, Y. Jiang, H. Pu, Z. Wu, X. Xu, Z. Zhao, J. Liu, X. Lu, X. Liu, B. Li, An H2S-BMP6 dual-loading system with regulating yap/Taz and Jun pathway for synergistic critical limb ischemia salvaging therapy, Adv. Healthc. Mater. 12 (28) (2023) 2301316, https://doi.org/10.1002/adhm.202301316.